Journal of Power Sources 241 (2013) 311–319

Contents lists available at SciVerse ScienceDirect

Journal of Power Sources

journal homepage: www.elsevier.com/locate/jpowsour

Thermal and electrochemical stability of organosilicon electrolytes for lithium-ion batteries

Xin Chen [a], Monica Usrey [b], Adrian Peña-Hueso [b], Robert West [a,b], Robert J. Hamers [a,b,*]

[a] Department of Chemistry, University of Wisconsin-Madison, 1101 University Avenue, Madison, WI 53706, United States
[b] Silatronix, Inc, 3587 Anderson Street, Suite 108, Madison, WI 53704, United States

HIGHLIGHTS

- 1NM3 + $LiPF_6$ is stable to nearly 100 °C, and potentials of 4.5 V at room temperature.
- The limiting stability of 1NM3 + $LiPF_6$ is the $LiPF_6$ salt.
- Decomposition induced by PF_5, not by fluoride, and occurs by cleavage of Si–O bond.
- SEI layers formed on graphite anodes contain no silicon.
- SEI layers formed from the ethylene glycol groups.

ARTICLE INFO

Article history:
Received 17 February 2013
Received in revised form
15 April 2013
Accepted 15 April 2013
Available online 20 April 2013

Keywords:
Electrolyte
Organosilicon
Lithium-ion battery
Hydrolysis
Thermal stability

ABSTRACT

Organosilicon (OS) electrolytes that integrate an ethylene glycol oligomer with a trimethylsilane head group are promising substitutes for commercial carbonate-based electrolytes because of their low flammability and their high electrochemical and thermal stability. To explore the factors that control thermal and electrochemical stability of these compounds, we developed a real-time headspace analysis apparatus with a mass spectrometer to detect the evolution of decomposition products during thermal cycling and during electrochemical measurements. Here we present mass spectroscopy, XPS, and SEM results exploring the thermal stability of [2-[2-(2-Methoxyethoxy)ethoxy]ethoxy]trimethylsilane (1NM3) with $LiPF_6$, and its electrochemical stability against graphite anodes and $LiCoO_2$ cathodes. Our results show that 1NM3 + $LiPF_6$ shows no significant decomposition below 100 °C and at potentials below 4.5 V. At higher temperatures and/or potentials, decomposition of $LiPF_6$ induces hydrolysis of 1NM3. Our results show that $LiPF_6$ decomposition is the limiting factor controlling stability of 1NM3 + $LiPF_6$ electrolytes and also provide fundamental insights into the molecular bonds of 1NM3 that are attacked by PF_5 and its decomposition products. Full-cell measurements of 1NM3 + $LiPF_6$ + vinyl carbonate show Coulombic efficiencies of >99.6%. These results point the way to new molecular structures that may have even further enhanced electrochemical and thermal stability.

1. Introduction

Lithium-ion batteries (LIBs) are one of the most popular energy storage components for portable electronics due to their high energy and power densities [1,2]. The increasing interest in automotive applications such as electric vehicles (EV) and hybrid electric vehicles (HEV) has led to increasing concern about the flammability of traditional carbonate-based electrolytes [3]. Organosilicon compounds have emerged as a novel class of materials with a number of unusual properties, including high electrochemical and thermal stability, high dielectric constants, high ionic conductivity (>10^{-3} S cm^{-1} with lithium salt added), and low viscosity [4–7]. Moreover, their low flammability suggests they may be good alternatives to more commonly used carbonate solvents, ethylene carbonate (EC), diethyl carbonate (DEC) and dimethyl carbonate (DMC). Among them, [2-[2-(2-Methoxyethoxy)ethoxy]ethoxy]trimethylsilane, also known as 1NM3 (structure shown in Fig. 1), has a low viscosity (1.4 cP at 300 K), moderate dielectric constant (5.13), and high ionic conductivity (1.8 mS cm^{-1} at 25 °C with 1.2 M LiTFSI salt) [4]. 1NM3 has also been shown to have good cycling characteristics when used with LiBOB salt [4].

* Corresponding author. Department of Chemistry, University of Wisconsin-Madison, 1101 University Avenue, Madison, WI 53706, United States.
E-mail address: rjhamers@wisc.edu (R.J. Hamers).

0378-7753/$ – see front matter © 2013 Elsevier B.V. All rights reserved.
http://dx.doi.org/10.1016/j.jpowsour.2013.04.079

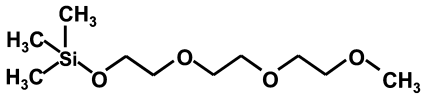

Fig. 1. Molecular structure of 2,2-dimethyl-3,6,9,12-tetraoxa-2-silatridecane (1NM3).

While 1NM3 and related organosilicons have been shown to have good performance characteristics with LiTFSI and LiBOB [4,6,7], the performance of 1NM3 with the industry-standard $LiPF_6$ salt has not been reported previously. $LiPF_6$ is the most commonly used salt for lithium ion batteries because it is highly soluble in organic electrolytes and yields good ionic conductivity (>10 mS cm^{-1}, while also being resistant to Al corrosion [8]). However, the major drawback of $LiPF_6$ comes from the reaction: $PF_6^- \rightarrow F^- + PF_5$ which creates increasing amounts of PF_5 at elevated temperatures (>60 °C) [9,10]. Previous studies have shown that the F^- and PF_5 products can react with solvents and other additives in the electrolyte and the electrodes, resulting in growth of the SEI film on the surface of electrode particles [11].

The reaction mechanism between $LiPF_6$ and carbonate solvents has been studied extensively [12–15] using a variety of techniques including differential scanning calorimetry (DSC) [12,14–16], accelerated rate calorimetry (ARC) [14,16], nuclear magnetic resonance (NMR) [13,17] and gas chromatography (GC) [9], infrared spectroscopy [18] and gas chromatography/mass spectroscopy [19]. Through these studies, it has generally concluded that decomposition is induced by reaction of PF_5 with trace amounts of alcohols or water to form POF_3, which then catalytically decomposes the carbonate electrolytes [13].

In this paper, we present a detailed description of the thermally and electrochemically induced decomposition of the organosilicon molecule 1NM3 with the industry-standard $LiPF_6$ salt, using a real-time headspace analysis setup with mass spectrometry. This method has been developed to allow us to detect the evolution of gas-phase decomposition products at specific temperatures during thermal cycling or at specific potentials during electrochemical measurements, and avoid the risk of reacting with air and water in transferring processes. We further demonstrate that the Lewis base additive dimethyl acetamide (DMAc) can enhance the stability of $LiPF_6$-based organosilicon electrolyte. Our results demonstrate that the stability of 1NM3 is limited by decomposition of the salt and demonstrate the mechanism by which the organosilicon compound decomposes. The resulting insights can potentially guide the synthesis of new, more stable compounds.

2. Experimental

2.1. Chemicals and electrodes

In these studies 2,2-dimethyl-3,6,9,12-tetraoxa-2-silatridecane (1NM3) was synthesized and purified to >99.8% as reported previously [4]. Lithium hexafluorophosphate ($LiPF_6$), tetramethylammonium fluoride, and dimethyl acetamide (DMAc) were purchased from Sigma–Aldrich. All electrolytes were stored in an Argon-purged glove box. Electrochemical Karl Fischer titration measurements of the water content yielded values of <15 parts per million in all of the electrolytes have been used. A conductivity of 1.8 mS cm^{-1} was measured. For the electrodes we used a commercial $LiCoO_2$ cathode (one side coated, capacity 1.5 mAh cm^{-2}; Piotrek Co., Ltd.), a Piotrek graphite anode (one side coated, capacity 1.6 mAh cm^{-2}; Piotrek Co., Ltd.) without modification and a Li ribbon (0.38 mm thickness, 99.9%, Sigma–Aldrich). The $LiCoO_2$ cathode had 26.8 mg cm^{-2} of active material and a capacity of 1.5 mAh cm^{-2}. The theoretical capacity of the graphite anode was 1.6 mAh cm^{-2}, or 291 mAh g^{-1} of active material. The separator material is a surfactant-coated polypropylene (Celgard® 3400) membrane with a 25 μm thickness.

2.2. Thermally controlled real-time headspace analysis with mass spectrometry

The temperature of the electrolyte was controlled used a programmable temperature controller (PTC 10, Stanford Research Systems). Electrolyte and the electrode materials were placed into glass sample vial. Argon gas (at a flow rate of ~0.4 ml min^{-1} at atmospheric pressure) passed over the sample and was then continuously sampled using a universal gas analyzer (UGA100, Stanford Research Systems). The mass spectra of the gas-phase species were recorded at 5 °C intervals and typically averaged over 3 scans taken from 1 to 200 amu.

2.3. Electrochemically controlled real-time headspace analysis with mass spectrometry

All cell assembly operations were conducted in an Argon glove box with less than 10 parts per million (ppm) water. A two-electrode cell was fabricated by soaking the separator (16.15 mm diam.) in the electrolyte and sandwiching this between the $LiCoO_2$ working electrode (16.15 mm diam.) and lithium reference electrode (15 mm diam.). The electrode assembly was crimp-sealed in a standard 2032 stainless steel coin cell in which a small hole (1 mm in diameter) was previously punched; the complete assembly was then sealed in a Teflon holder with a sealed capillary (1/64 inch inside diameter, 1/16 inch outside diameter) that formed the input to the a universal gas analyzer (UGA100, Stanford Research Systems). Two-electrode cyclic voltammograms were measured using a Solar 1287 potentiostat. Each anodic scan was swept from the open circuit potential (OCP) to 0.1 V vs. Li/Li^+ and then back to 3 V vs. Li/Li^+ at 1 mV s^{-1}. Each cathodic scan was swept from the open circuit potential (OCP) to 7 V vs. Li/Li^+ at 1 mV s^{-1}. Mass spectra of the gas-phase species were recorded at 0.1 V intervals, averaged over 3 scans covering the range from 1 to 200 amu.

2.4. Surface analysis

The dry graphite electrode was imaged using scanning electron microscopy (SEM, LEO Supra 55VP) at 1 kV incident electron energy and a 4 mm working distance. X-ray photoelectron spectroscopy (XPS) measurements were carried out in an ultra-high vacuum system ($P < 5 \times 10^{-10}$ torr) equipped with a load-lock for sample introduction, a monochromatized Al Kα source (1486.6 eV) and a hemispherical analyzer with a 16-channel detector array. All spectra were collected at 45° photoelectron take-off angles. All the core peaks were calculated by fitting the area under the XPS component peaks using Voigt functions with a baseline correction.

3. Results

3.1. Thermal stability of 1NM3

Fig. 2 shows gas-phase mass spectra of the headspace above a sample of pure 1NM3 (with no salt) at 30 °C and 150 °C. The mass spectra of the gas-phase species are nearly identical for these two cases. From 2 to 44 amu there are several peaks present that arise from the Argon flow and from small amounts of residual air in the mass spectrometer. These include H_2^+ (2 amu), H_2O^+ (18 amu), Ar^{2+} (20 amu), N_2^+ (28 amu), O_2^+ (32 amu), $^{36}Ar^+$ (36 amu), Ar^+ (40 amu) and CO_2^+ (44 amu). Measurement of the headspace for the sample heated to 150 °C shows that these peaks are again present with

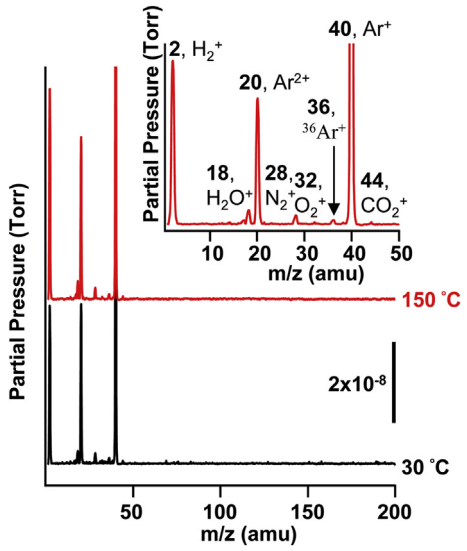

Fig. 2. Mass spectra of gas-phase species evolved from cells containing 1NM3 (without added salt) at 30 °C and 150 °C.

nearly identical intensity; no additional peaks are observed within the sensitivity limits of the mass spectrometer.

3.2. Thermal stability of 1NM3 with $LiPF_6$

Fig. 3 shows how the head-space mass spectra of 1NM3 + 1 M $LiPF_6$ vary as a function of temperature. The mass spectra remain quite similar at $m/z < 44$ amu even when the temperature is increased to above 100 °C. No detectable change is observed at $m/z > 44$ amu below 100 °C (Fig. 3a), however, at ~100 °C, a new peak at 77 amu is observed, along with smaller peaks at $m/z = 48$, 49, 63, 92, and 147 amu (Fig. 3b). The intensity of each peak increases as the electrolyte is heated to higher temperatures until it begins to boil at 115 °C. The peak at 77 amu is attributed to $Si(CH_3)_2F^+$, while the other peaks are attributed to $SiHF\bullet^+$ (48 amu), SiH_2F^+ (49 amu), $SiH(CH_3)F^+$ (63 amu), $Si(CH_3)_3^+$ (73 amu), $Si(CH_3)_3F\bullet^+$ (92 amu) and $(CH_3)_3SiOSi(CH_3)_2^+$ (147 amu).

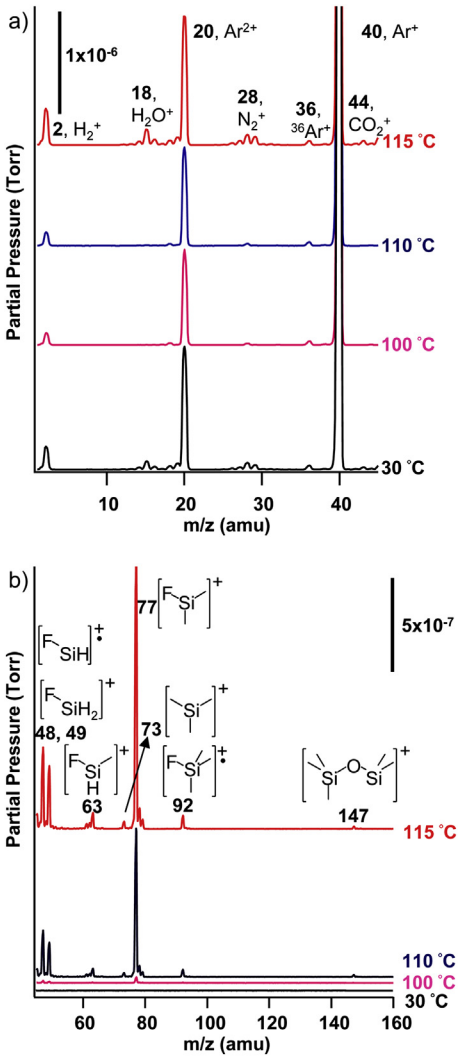

Fig. 3. Mass spectra of gas-phase species evolved from cells containing 1NM3 + 1 M $LiPF_6$ at 30 °C and temperature above 100 °C at $m/z < 44$ amu (a) and $m/z > 44$ amu (b).

3.3. Effect of decomposition products of $LiPF_6$ on thermal stability of 1NM3 + $LiPF_6$

Since several of the observed peaks arise from species containing fluorine, we conducted additional experiments in order to understand how these species are formed, and particularly to identify the roles of F^- and of PF_5. To distinguish between these two, we first added excess F^- to the solution, by addition of 0.1 M tetramethylammonium fluoride (TMABF) into the 1NM3 + 1 M $LiPF_6$ solution. As shown in Fig. 4a, headspace analysis shows that F^- containing species are observed when the sample is heated above 100 °C, but the fragmentation patterns and intensities are nearly identical to those observed in Fig. 3b for the sample lacking excess F^-. This shows that the addition of fluoride ion has no significant effect on the thermochemistry.

To confirm that the excess F^- was not all sequestered as LiF, we also performed a similar experiment using 1NM3 + 0.1 tetramethylammonium fluoride, with no $LiPF_6$ present. The result in Fig. 4b showed little reactivity even at high temperature up to 150 °C, as the intensity of the peaks is much smaller (10^{-9} torr at the mass spectrometer input) than what is observed with $LiPF_6$ present. Thus, we conclude that F^- has little effect on the thermal stability of 1NM3.

Since PF_5 is a gaseous reactant, we did not attempt to introduce this compound directly into the electrolyte. Instead, we relied on the fact that previous studies have shown that dimethyl acetamide (DMAc) forms a stable adduct with PF_5, sequestering it and preventing it from reaction with carbonate electrolytes [17]. Thus, the addition of DMAc to the electrolyte will reduce the amount of PF_5 present. Fig. 4c shows head-space mass spectra after addition of 0.1% (by volume) of DMAc into 1NM3 + 1 M $LiPF_6$. In this case the mass spectra show tiny amount of product in 10^{-8} torr level at $m/z = 77$ amu at $T = 110$ °C. Larger intensity is observed at $m/z = 77$ amu when heated to higher temperature and finally significant decomposition is observed at 130 °C with the onset of boiling.

Fig. 5 shows the intensity of the $m/z = 77$ amu peak for the three solutions described above. The plot for 1NM3 + $LiPF_6$ + tetramethylammonium fluoride is nearly identical to that of 1NM3 + $LiPF_6$ (Fig. 5a), with no significant intensity at temperatures below 100 °C but increasing rapidly at higher temperatures. In contrast, the graph for 1NM3 + $LiPF_6$ + DMAc shows no significant intensity below 120 °C, which is close to the boiling point, and even at the boiling point the peak at 77 amu has an intensity only ~15% of that observed with 1NM3 + $LiPF_6$. With enlarged view in Fig. 5b, it is quite clear that 1NM3 + tetramethylammonium fluoride

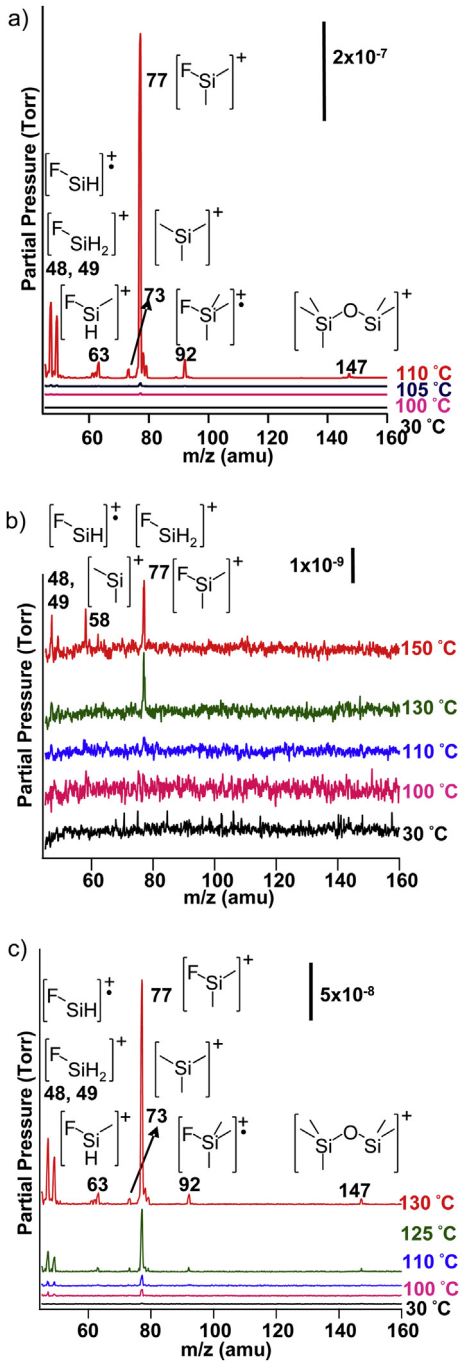

Fig. 4. Mass spectra of gas-phase evolved from cells containing (a) 1NM3 + 1 M $LiPF_6$ + 0.1 M tetramethylammonium fluoride, (b) 1NM3 + 0.1 M tetramethylammonium fluoride and (c) 1NM3 + 1 M $LiPF_6$ + 0.1% dimethyl acetamide (DMAc) at 30 °C and temperature above 100 °C.

sample shows an increase in peak intensity at 77 amu above 110 °C, but only to the 10^{-9} torr level.

3.4. Effect of trace water in thermal stability of 1NM3 + $LiPF_6$

To better understand whether the $(CH_3)_3SiOSi(CH_3)_2^+$ at 147 amu is a product from the fluorination or hydrolysis reaction with trace water present in the electrolyte, we performed two control experiments adding 500 ppm H_2O to 1NM3 itself or the one with 1 M $LiPF_6$ dissolved. Fig. 6a shows the evolution of the headspace mass spectra of 1NM3 + 500 ppm H_2O with increasing

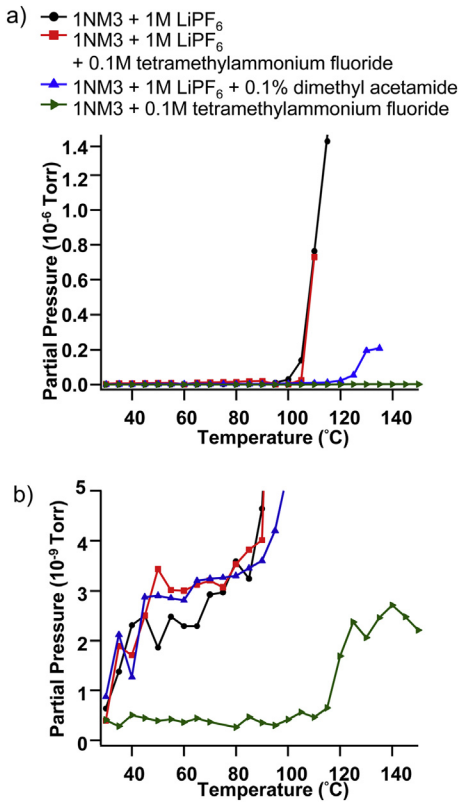

Fig. 5. Comparison of peak intensity at 77 amu in mass spectrum vs. temperature for 1NM3 + 1 M $LiPF_6$, 1NM3 + 1 M $LiPF_6$ + 0.1 M tetramethylammonium fluoride, 1NM3 + 0.1 M tetramethylammonium fluoride and 1NM3 + 1 M $LiPF_6$ + 0.1% dimethyl acetamide (DMAc). Note that the scale in b is 1000× more sensitive than that in a.

temperature; this spectrum is quite clean without any new decomposition peaks showing up at high temperature up to 150 °C. With dissolved $LiPF_6$ in the 1NM3, adding 500 ppm H_2O to the solution shows similar new peaks when heated up above 100 °C till boiling at 115 °C, but the peak intensities at 147 amu are much greater than those observed in the 1NM3 + 1 M $LiPF_6$ sample.

3.5. Electrochemical stability at graphite electrode

Fig. 7a shows the voltammogram of a graphite electrode vs. lithium reference using 1NM3 + 1 M $LiPF_6$ as the potential is brought from the initial open-circuit potential 2.1 V down to 0.1 V, up to 3.0 V, and then back to 2.1 V, at a rate of 1 mV s^{-1}. The graph shows a reduction peak at 0.75 V vs. Li/Li^+. Mass spectra were obtained each 0.1 V during this experiment. Fig. 7b and c show mass spectra obtained at several selected potentials. The mass spectrum gas-phase species from the coin cell in the cyclic voltammogram scan shows no new peaks or intensity change. Some very narrow noise spikes occur in the very high-sensitivity spectrum in Fig. 7c (for example, at $m/z \sim 78$ in the 0.2 V spectrum) and are identified as noise spikes because their width is narrower than the mass spectrometer resolution.

Fig. 8a shows scanning electron microscope images of a fresh graphite-based anode and one that was cycled using this same cyclic voltammogram procedure. On the fresh sample, the active graphite material can be observed, along with tiny clusters present on the particle surfaces from the polymer binder, conductive carbon black, or additives used in the anode preparation process. After the CV scan, the SEM images reveal a surface that appears slight rougher (Fig. 8b), but which otherwise has no drastic changes in

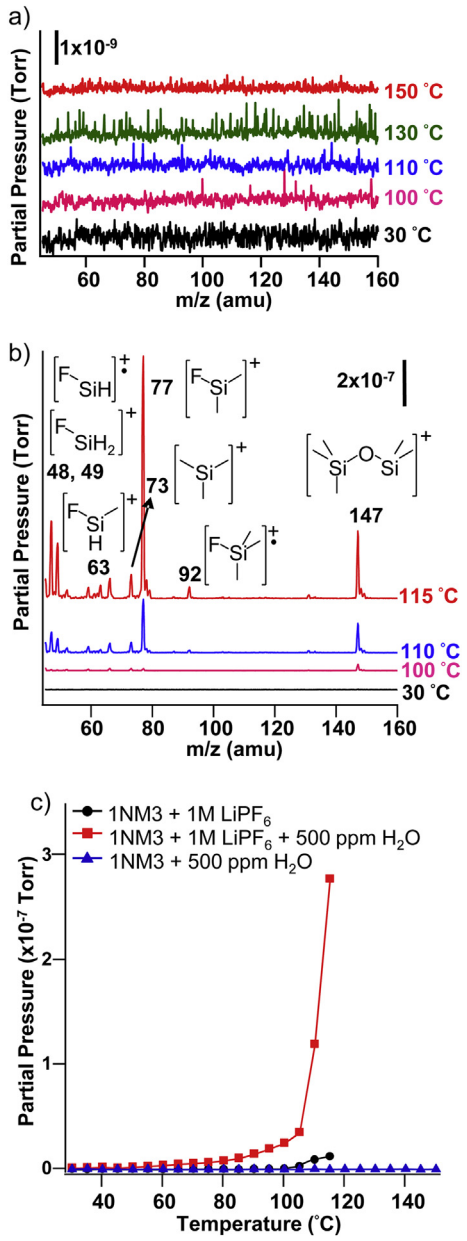

Fig. 6. (a) Mass spectra of gas-phase evolved from cells containing 1NM3 + 500 ppm H_2O; (b) Mass spectra of gas-phase evolved from cells containing 1NM3 + 1 M $LiPF_6$ + 500 ppm H_2O and (c) Comparison of peak intensity at 147 amu in mass spectrum vs. temperature for 1NM3 + 1 M $LiPF_6$, 1NM3 + 500 ppm H_2O and 1NM3 + 1 M $LiPF_6$ + 500 ppm H_2O.

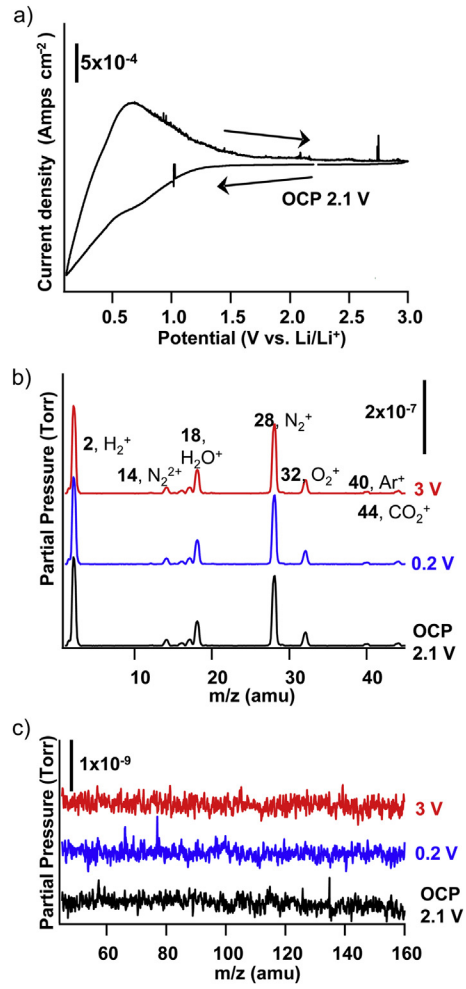

Fig. 7. (a) Cyclic voltammogram plot for 1NM3 + 1 M $LiPF_6$ on the graphite surface; (b) Mass spectra have been recorded simultaneously with cyclic voltammogram scan for 1NM3 + 1 M $LiPF_6$ at open circuit potential (OCP), at 0.2 V vs. Li/Li^+ and at 3 V vs. Li/Li^+ (c) Same as (b) except higher mass range.

morphology. Fig. 8c shows selected XPS results from the same electrodes. Additional XPS spectra for other elements are included in the Supplemental Information. The atomic percentages of each element are shown in Table 1. These are calculated as:

$$\text{Atomic percentage of element } X \text{ is given by } \frac{100(A_X/S_X)}{\sum_i A_i/S_i}$$

where A_i is the XPS peak area of the ith element, and S_i is the XPS sensitivity factor for that element.

The C(1s) spectrum of the fresh anode is easily deconvoluted into 3 peaks at 284.6, 286.4 and 291.0 eV. The peak at 284.6 eV arises from bulk graphite, and the peak at 286.4 eV arises from C—O species [20]. The peak at 291 eV arises from C—F species of the binder material and may also contain small contributions from the "shake-up" satellite of bulk graphite [21]. After the CV scan, peaks are observed at 286.4 eV, 288.4 eV and 291.7 eV. The changes in peak energies and intensities arise from a combination of chemical shifts and charging. Because lithiation decreases the work function of the graphite, the secondary electron yield becomes higher and charging of the sample shifts all peaks to slightly higher binding energy. By comparing the corresponding shifts in C(1s) with those of the F(1s) and O(1s) peak (not shown) and also by comparing the peaks observed here with those we observed previously for ethylene glycol oligomers on diamond [22] we determined that charging effect increased the binding energy of the "after CV scan" peaks by ~1.4 eV compared to the fresh sample. Detailed interpretation of the XPS spectra is complicated by the complicated spatial heterogeneity of the electrode. However, after lithiation the C(1s) spectrum shows a new peak 288.4 eV that arises from the ethylene glycol groups; this peak dominates the C(1s) spectrum. The presence of this peak shows that decomposition of 1NM3 leaves behind a surface film comprised of ethylene glycol chains on the surface. Perhaps more surprisingly, the Si(2p) spectrum shows only a very small amount of silicon, only ~2 atomic% compared with 25 atomic% from the ethylene glycol C(1s) peaks; while based on the molecular structure (Fig. 1) there are 7 ether-like C atoms per Si atom in the parent molecule, the small amount of Si in the surface film indicates that most molecules have the Si—O—C

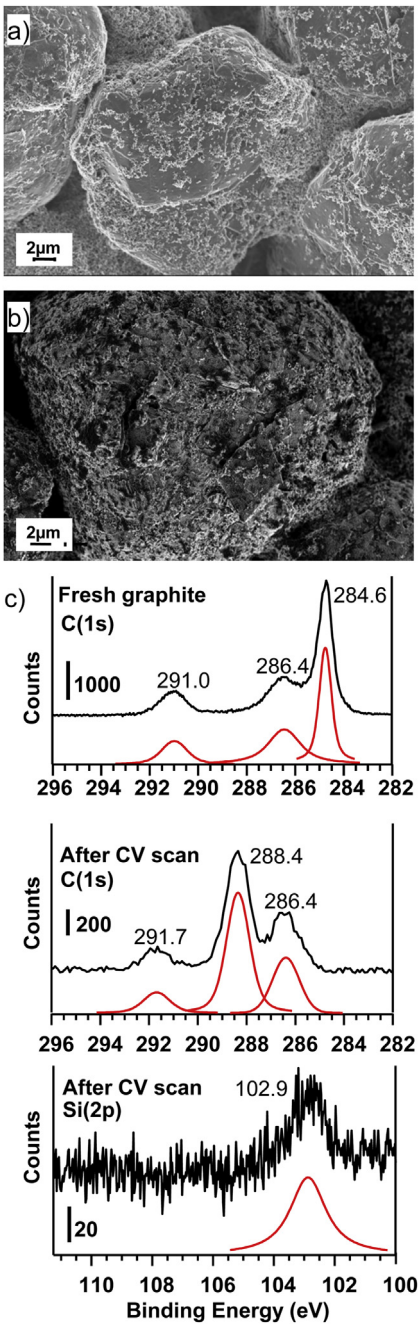

Fig. 8. (a) Scanning electron microscope (SEM) image of the fresh graphite electrode; (b) Scanning electron microscope (SEM) image of the graphite electrode after the cyclic voltammetry scan; (c) X-ray photoelectron C(1s) spectra of the fresh graphite electrode and the C(1s) and Si(2p) regions of the graphite electrode after the cyclic voltammetry scan.

bond cleaved with only the glycol molecule remaining on the surface, with the Si-containing portion leaving as gas-phase products.

3.6. Electrochemical stability at $LiCoO_2$ electrode

Fig. 9a shows the cathodic voltammogram on $LiCoO_2$ electrode vs. lithium reference using 1NM3 + 1 M $LiPF_6$ and 1NM3 + 1 M $LiPF_6$ + 1% dimethyl acetamide (DMAc). For the 1NM3 + $LiPF_6$ sample, the current begins to increase rapidly above 4.5 V vs. Li/Li^+, and shows fluctuating current above 5.5 V vs. Li/Li^+. When the same experiment is performed using electrolyte including 1%

Table 1
Binding energy (eV) and atomic percentages (%) of the components of a fresh graphite electrode, and the graphite electrode after the anodic CV scan using electrolyte 1NM3 + 1 M $LiPF_6$.

	Fresh graphite		After CV	
			1NM3 + $LiPF_6$	
C 1s	284.6	31.3%	286.4	11.3%
	286.4	36.8%	288.4	24.5%
	291	19.9%	291.7	4.7%
F 1s	689	6.2%	689.8	21.1%
O 1s	532.9	1.7%	533.9	15.0%
	534.8	4.4%	535.4	17.8%
P 2p	–	–	137.7	3.3%
Si 2p	–	–	102.9	2.1%

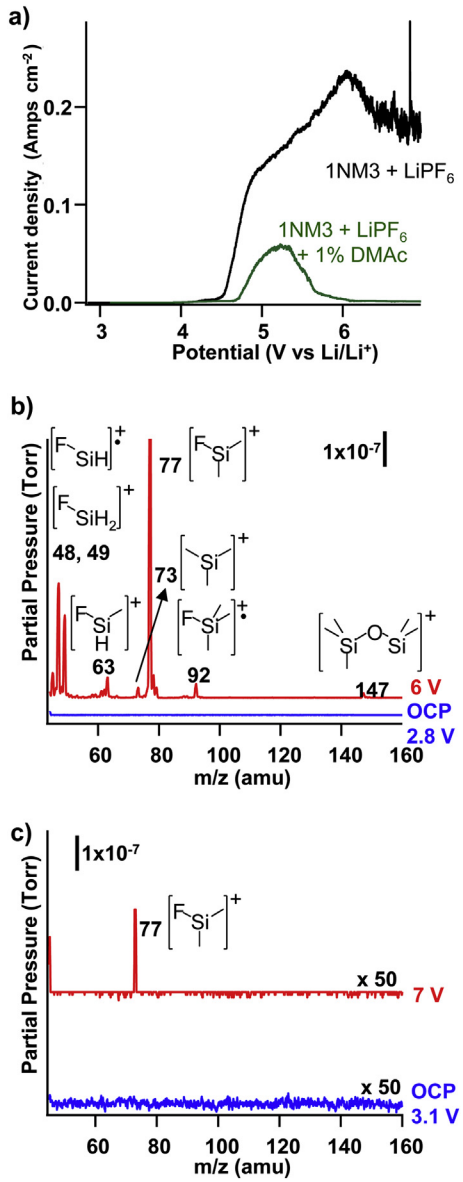

Fig. 9. (a) Cyclic voltammogram plot for 1NM3 + 1 M $LiPF_6$ and 1NM3 + 1 M $LiPF_6$ + 1% dimethyl acetamide (DMAc) on the $LiCoO_2$ surface; (b) Mass spectrum has been recorded simultaneously with cyclic voltammogram scan for 1NM3 + 1 M $LiPF_6$ at open circuit potential (OCP) and at 6 V vs. Li/Li^+; (c) Mass spectrum has been recorded simultaneously with cyclic voltammogram scan for 1NM3 + 1 M $LiPF_6$ + 1% dimethyl acetamide (DMAc) at open circuit potential (OCP) and at 7 V vs. Li/Li^+.

dimethyl acetamide (DMAc), the cathodic current shows a broad peak from 4.7 to 6 V vs. Li/Li^+. The introduction of DMAc extends the stability window by ~0.2 V and also appears to greatly limit the current at very high potentials.

The corresponding mass spectra at selected potentials using 1NM3 + 1 M $LiPF_6$ and using 1NM3 + 1 M $LiPF_6$ + 1% DMAc are shown in Fig. 9b and c. With 1NM3 + 1 M $LiPF_6$ as the electrolyte, new peaks are observed in the headspace when the potential is increased to 6 V vs. Li/Li^+. The relative intensities of the peaks at m/z = 48 amu ($SiHF•^+$), m/z = 49 amu (SiH_2F^+), m/z = 63 amu ($SiH(CH_3)F^+$), m/z = 73 amu $Si(CH_3)_3^+$, m/z = 77 amu ($Si(CH_3)_2F^+$), m/z = 92 amu ($Si(CH_3)_3F•^+$) and m/z = 147 amu $(CH_3)_3SiOSi(CH_3)_2^+$ are nearly identical to those observed in the thermal experiments shown in Figs. 3 and 4. However, the sample containing DMAc shows only very little gas evolution (note that the spectra in Fig. 9c have been expanded 50× compared with those in Fig. 4c) at m/z = 77 amu, and only shows up at high potentials at 7 V vs. Li/Li^+.

3.7. Charge–discharge performance characteristics

To examine the characteristics of 1NM3 in a full cell, we fabricated coin cells using Piotrek graphite vs. $LiCoO_2$ and tested the performance of 1NM3 + $LiPF_6$ and also of 1NM3 + $LiPF_6$ + 2% vinyl carbonate (by volume) in a standard 2032 coin cell. We used four formation cycles at C/10 charge (0.3 mA) and C/20 discharge (0.15 mA), followed by 50 cycles at C/4 charge and C/4 discharge (0.75 mA). Fig. 12 shows the resulting discharge capacities and Coulombic efficiencies. The cells consisting of 1NM3 + $LiPF_6$ alone, without any additional additives, show relatively poor performance, with low Coulombic efficiency. This suggests, in agreement with the above results, that the high electrochemical stability of 1NM3 leads to a poor quality SEI layer unless additional additives are used. However, the addition of 2% vinyl carbonate as an additive greatly improves the performance, resulting in greatly improved Coulombic efficiencies. The decrease in discharge capacity from 200 mAh g^{-1} to 270 mAh g^{-1} from cycle 5 to cycle 50 for the sample containing 2% vinyl carbonate corresponds to an average Coulombic efficiency of 99.6%.over the 46 post-formation cycles. This suggests that a fully formulated electrolyte should be possible that will allow the high electrochemical and thermal stability of 1NM3 to be utilized to enhance the overall stability window of full electrochemical cells.

4. Discussion

Our data show that the organosilicon compound 1NM3 has excellent thermal stability and shows no evidence for decomposition when heated to 150 °C. When $LiPF_6$ salt is dissolved in 1NM3, the electrolyte continues to show excellent thermal stability up ~100 °C. At higher temperatures, decomposition products of $LiPF_6$ salt initiate reaction with 1NM3 molecules to produce several different fragments depicted in Fig. 3b. Notably, the detected fragments involve cleavage of Si–O bond, and most contain a single Si–F bond. Since the species at m/z = 48, 49, 63, 77, and 92 amu all have the same relative intensities, we conclude that they likely arise from a single common precursor.

The data show that the 1NM3 + $LiPF_6$ solutions with or without extra tetramethylammonium fluoride nearly identical thermal stabilities. From this we conclude that F^- does not induce 1NM3 decomposition reaction, and therefore that F^- from $LiPF_6$ decomposition is not the reactant in further reaction with 1NM3 molecules. Conversely, we observe a significant improvement in stability when dimethyl acetamide (DMAc) is added into 1NM3 + $LiPF_6$ electrolyte. Since the Lewis base character of DMAc allows it to sequester the free PF_5 species has been generated from $LiPF_6$ decomposition, we conclude that PF_5 is the primary reactant responsible for inducing reaction of 1NM3 to form the fluoride derivative and the hydrolysis reaction. Fig. 10 shows the reaction route of PF_5 with 1NM3 and Fig. 11 displays all the smaller fragments that be readily produced by fragmentation of trimethylfluorosilane (m/z = 92 amu) as a result of the electron-impact ionization scheme used in the mass spectrometer.

Notably, we do not observe any intensity at m/z = 107 amu (the most intense peak observed from electron impact ionization of PF_5) or m/z = 104 amu (the most intense peak from O=PF_3, the product of reaction of PF_5 with water) [23]. Previous studies of PF_6 thermal decomposition in carbonate solvents reported detecting PF_5 and (in the presence of water) O=PF_3 as gas-phase products via infrared spectroscopy [24]. Our results suggest that reaction of PF_5 with 1NM3 is sufficiently fast that it occurs before significant PF_5 is released into the headspace. Early work by Kifer and Van Dyke showed that PF_5 reacts rapidly with $(CH_3)_3$–Si–O–CH_3 to form $(CH_3)_3$–Si–F [25]. More recently, Sloop and co-workers showed that PF_5 can attack alkyl carbonates to form poly(ethylene glycol) oligomers that continue to be degraded by PF_5 [26]. These previous studies suggest that 1NM3 and related compounds with the general structure $(CH_3)_3$–Si–O–$(CH_2CH_2O)_nCH_3$ will be cleaved at the Si–O bond to form $(CH_3)_3$–Si–F and a transient F_4P–O$(CH_2CH_2O)_nCH_3$ species that likely undergoes rapid decomposition. The temperature at which we observed PF_5-induced decomposition (>100 °C) agrees well with prior work by Yang et al. [24].

In addition to the reaction with PF_5, our data indicate that there is additional reaction pathway that gives rise to peaks at m/z = 58, 66, 73 and 147 amu. The presence of the peaks from the sample of 1NM3 + 1 M $LiPF_6$ but not from the pure 1NM3 sample suggests that the hydrolysis peaks are associated with the presence of $LiPF_6$. Adding extra water to the 1NM3 + 1 M $LiPF_6$ results in much larger peak intensities at 58, 66, 73 and 147 amu but does not introduce these peaks if no $LiPF_6$ is dissolved in 1NM3 indicate that these peaks likely arise from acid-catalyzed hydrolysis of 1NM3 [27] and pathway is demonstrated in Fig. 10(iv–v). Since all the gas-phase species increase in intensity at the same temperature, it is likely that formation of the hydrolysis products is also initiated by PF_5 (or HF produced by reaction with trace amounts of water, via

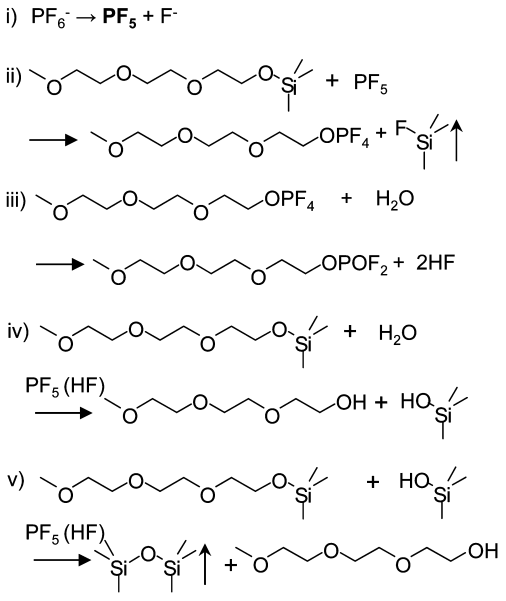

Fig. 10. Proposed fluorinated and hydrolysis reaction pathway of 1NM3 molecule with $LiPF_6$ salt in the presence of trace amounts of water.

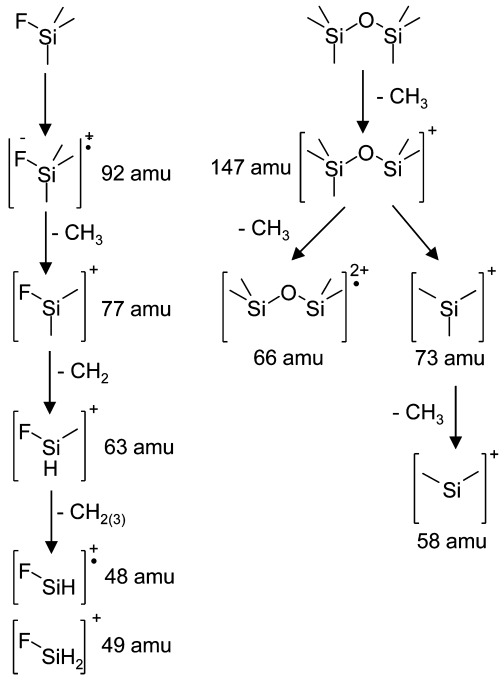

Fig. 11. Decomposition and fragmentation pathway of trimethylfluorosilane and hexamethyldisiloxane after electron-impact ionization in the mass spectrometer.

$PF_5 + H_2O \rightarrow POF_3 + 2HF$). Si–O–C bonds can be cleaved by water in the presence of acidic catalysts, and the subsequent re-coupling of the $(CH_3)_3$–Si–OH hydrolysis products would lead to $(CH_3)_3Si$–O–$Si(CH_3)_3$ with $m/z = 162$ amu. While we do not see a product at this m/z ratio, loss of a methyl group due to fragmentation during electron impact would produce $[(CH_3)_3Si–O–Si(CH_3)_2]^+$ ($m/z = 147$ amu) which can further decompose to $[(CH_3)_3Si–O–Si(CH_3)_2]^+$ ($m/z = 147$ amu). Indeed, literature spectra of $(CH_3)_3Si–O–(CH_3)_3$ show little or no intensity from the parent ion at $m/z = 162$ amu and show the peak at 147 amu to be the largest peak in the spectrum, followed by $m/z = 73$, 66 and 58 amu [28], in good agreement with our observations.

The products we observe experimentally are quite different from those recently predicted by Assary et al. for oxidation of 1NM3-like molecules in the absence of salt [29]. According to their calculations, the most stable products are formed via cleavage of the C–O and C–C bonds, not the Si–O bond. However, we do not observe any fragments corresponding to C–C or C–O bond fragmentation. This again highlights that under the conditions used here with $LiPF_6$ salt, the overall reaction pathways are controlled by the salt and its decomposition products, not by the 1NM3 electrolyte itself.

4.1. Electrolyte behavior under reducing conditions

The electrochemical measurements in Fig. 7 show that under reducing conditions (i.e., electrode potentials of <3 V vs. Li/Li^+) there are some decomposition reactions taking place in the cell but no evolution of identifiable gas-phase products. Previous studies have found that glyme-based electrolytes have reduction potentials more negative than Li/Li^+ [30]. Consequently, direct electrochemical reduction of 1NM3 is unlikely.

This conclusion is further supported by the XPS data in Fig. 8c; these data show that the distribution of surface species formed during the first formation cycle has a relatively high degree of fluorination, along with the incorporation of some phosphorus into the film. These results suggest that the SEI layer is formed in part by reduction of the PF_6^- anion. This conclusion is further supported by recent calculations of the electrochemical stability window of PF_6^- containing ionic liquids; these calculations predict that PF_6^- is not stable at the potential of Li/Li^+ [31]. Since our XPS studies show that the SEI layer has almost no Si in it (Fig. 8d), these data suggest that the reduction of PF_6^- likely leads to products such as $CH_2FCH_2O(CH_2CH_2O)_2CH_3$ that are deposited on the surface.

The cyclic voltammogram shows evidence for electrochemical reactions and XPS spectra of the graphite surface show that the graphite is covered with a solid–electrolyte interphase (SEI) layer. While we cannot rule out the evolution of small amounts of H_2 or H_2O (due to the presence of some background concentrations of these in the mass spectrometer), gas evolution appears insignificant. The charge–discharge data in Fig. 12 show that the SEI layer formed by 1NM3 + $LiPF_6$ without additional additives (such as vinyl carbonate) yields poor performance in full coin cells. However, dramatically improved performance can be achieved by incorporating vinyl carbonate as an additive. These results show that the very high electrochemical stability of 1NM3 + $LiPF_6$ results in poor-quality SEI layers; addition of vinyl carbonate greatly improves the stability by providing an additional pathway to electrochemical breakdown.

While 1NM3 + $LiPF_6$ shows great stability against graphite and against $LiCoO_2$ at potentials up to 4.2 V, at higher potentials decomposition products are observed on the $LiCoO_2$ surface. Notably, the relative intensities of the oxidation-induced peaks observed at potentials of >4.5 V vs. Li/Li^+ in the electrochemical measurements are nearly identical to those observed in the thermal experiments. Furthermore, the addition of DMAc greatly reduces gas evolution. Perhaps more significantly, the addition of DMAc significantly reduces the electrochemical currents as well. This

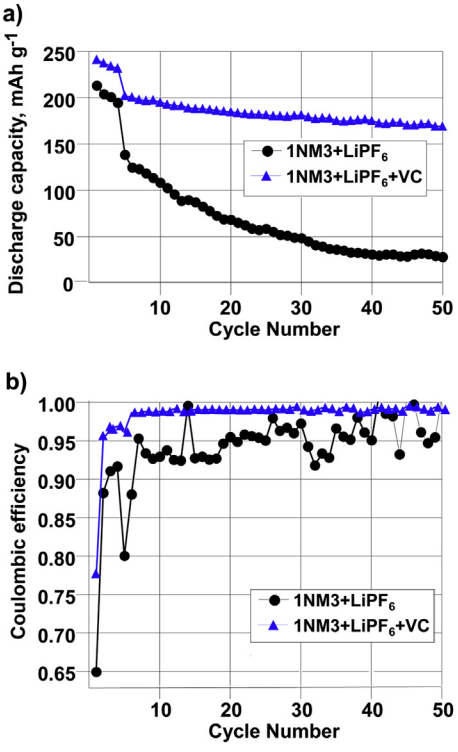

Fig. 12. Discharge capacity and Coulombic efficiency for full cell, Piotrek graphite vs. $LiCoO_2$, for 1NM3 + 1 M $LiPF_6$ and for 1NM3 + 1 M $LiPF_6$ + 2% (by volume) vinyl carbonate. Cells were charged to 4.2 V and discharged to 3 V, based upon data from the electrode manufacturer. Four SEI formation cycles at C/10 charge (0.3 mA) and C/20 discharge (0.15 mA) were followed by a minimum of 50 regular cycles at C/4 charge (0.75 mA) and C/4 discharge (0.75 mA).

suggests that the role of DMAc is more complex than simply trapping PF_5 formed via oxidation of PF_5.

5. Conclusions

The use of thermal/electrochemical real-time headspace analysis coupled with mass spectroscopy provides useful insights into the factors controlling the thermal and electrochemical stability of electrolytes. Our results show that the decomposition of electrolytes based on 1NM3 with the industry-standard $LiPF_6$ salt is controlled primarily by PF_5 that is formed by decomposition of the PF_6 anion. Decomposition of $LiPF_6$ produces PF5, which fluorinates 1NM3 molecules and catalyzes decomposition of 1NM3 hydrolysis reaction at high temperature (above 100 °C) and at high potentials vs. Li/Li^+. The addition of DMAc, a scavenger for PF5, stabilizes the electrolyte and reduces the thermal and electrochemical decomposition. The use of real-time mass spectroscopy provides new insights into the interaction of organosilicon compounds with lithium salts, other additives, and electrode materials for lithium ion batteries. While 1NM3 + $LiPF_6$ alone yields poor charge–discharge performance, with the simple addition of vinyl carbonate the Coulombic efficiency can exceed 99.6% in full cells. The introduction of additional additives will likely improve this performance even further. The may provide useful insights into the design of new electrolytes with improved thermal and electrochemical stability, enabling lithium-ion battery operation at higher temperatures and compatibility with high-voltage cathode materials.

Conflict-of-interest statement

Robert Hamers and Robert West are co-founders of Silatronix and have a financial interest in the outcome of this work.

Acknowledgment

This work was supported by the National Science Foundation Grant SBIR grant #0724469 to Silatronix, Inc.

Appendix A. Supplementary material

Supplementary material associated with this article can be found, in the online version, at http://dx.doi.org/10.1016/j.jpowsour.2013.04.079.

References

[1] J.B. Goodenough, J. Solid State Electrochem. 16 (2012) 2019–2029.
[2] T.H. Kim, J.S. Park, S.K. Chang, S. Choi, J.H. Ryu, H.K. Song, Adv. Energy Mater. 2 (2012) 860–872.
[3] E. Quartarone, P. Mustarelli, Chem. Soc. Rev. 40 (2011) 2525–2540.
[4] L. Zhang, Z. Zhang, S. Harring, M. Straughan, R. Butorac, Z. Chen, L. Lyons, K. Amine, R. West, J. Mater. Chem. 18 (2008) 3713–3717.
[5] N.A.A. Rossi, Z.C. Zhang, Y. Schneider, K. Morcom, L.J. Lyons, Q.Z. Wang, K. Amine, R. West, Chem. Mater. 18 (2006) 1289–1295.
[6] H. Nakahara, M. Tanaka, S.Y. Yoon, S. Nutt, J. Power Sources 160 (2006) 645–650.
[7] H. Nakahara, S. Nutt, J. Power Sources 160 (2006) 1355–1360.
[8] S. Zhang, T. Jow, J. Power Sources 109 (2002) 458–464.
[9] S. Sloop, J. Pugh, S. Wang, J. Kerr, K. Kinoshita, Electrochem. Solid State Lett. (2001) A42–A44.
[10] T. Kawamura, S. Okada, J. Yamaki, J. Power Sources 156 (2006) 547–554.
[11] D. Aurbach, B. Markovsky, I. Weissman, E. Levi, Y. Ein-Eli, Electrochim. Acta 45 (1999) 67–86.
[12] G. Botte, R. White, Z. Zhang, J. Power Sources 97 (8) (2001) 570–575.
[13] C.L. Campion, W.T. Li, B.L. Lucht, J. Electrochem. Soc. 152 (2005) A2327–A2334.
[14] J. Gnanaraj, E. Zinigrad, L. Asraf, H. Gottlieb, M. Sprecher, M. Schmidt, W. Geissler, D. Aurbach, J. Electrochem. Soc. 150 (2003) A1533–A1537.
[15] T. Kawamura, A. Kimura, M. Egashira, S. Okada, J. Yamaki, J. Power Sources 104 (2002) 260–264.
[16] D. MacNeil, J. Dahn, J. Electrochem. Soc. 150 (2003) A21–A28.
[17] W. Li, C. Campion, B. Lucht, B. Ravdel, J. DiCarlo, K. Abraham, J. Electrochem. Soc. 152 (2005) A1361–A1365.
[18] X. Teng, F. Li, P. Ma, Q. Ren, S. Li, Thermochim. Acta 436 (2005) 30–34.
[19] K. Kumai, H. Miyashiro, Y. Kobayashi, K. Takei, R. Ishikawa, J. Power Sources 81 (1999) 715–719.
[20] L. El Ouatani, R. Dedryvere, C. Siret, P. Biensan, S. Reynaud, P. Iratcabal, D. Gonbeau, J. Electrochem. Soc. 156 (2009) A103–A113.
[21] D. Briggs, M. Seah, Practical Surface Analysis by Auger and X-ray Photoelectron Spectroscopy, Wiley, Chichester, New York, 1983.
[22] C. Stavis, T.L. Clare, J.E. Butler, A.D. Radadia, R. Carr, H.J. Zeng, W.P. King, J.A. Carlisle, A. Aksimentiev, R. Bashir, R.J. Hamers, Proc. Natl. Acad. Sci. U. S. A. 108 (2011) 983–988.
[23] S.E. Stein, in: P.J. Lindstrom, W.G. Mallard (Eds.), National Institute of Standards and Technology (2012). http://webbook.nist.gov (retrieved 19.08.12), Gaithersburg, MD.
[24] H. Yang, G.V. Zhuang, P.N. Ross, J. Power Sources 161 (2006) 573–579.
[25] E.W. Kifer, C.H. Van Dyke, Inorg. Chem. 11 (1972) 404–408.
[26] S.E. Sloop, J.B. Kerr, K. Kinoshita, J. Power Sources 119–121 (2003) 330–337.
[27] M. Cypryk, Y. Apeloig, Organometallics 21 (2002) 2165–2175.
[28] National Institute of Advanced Science and Technology Spectral Database for Organic Compounds, SDBS #5566, http://sdbs.riodb.aist.go.jp (accessed 19.08.12).
[29] R.S. Assary, L.A. Curtiss, P.C. Redfern, Z.C. Zhang, K. Amine, J. Phys. Chem. C 115 (2011) 12216–12223.
[30] T. Inose, D. Watanabe, H. Morimoto, S.I. Tobishima, J. Power Sources 162 (2006) 1297–1303.
[31] S.P. Ong, O. Andreussi, Y.B. Wu, N. Marzari, G. Ceder, Chem. Mater. 23 (2011) 2979–2986.